Materials Research Proceedings 41 (2024) 1171-1181 https://doi.org/10.21741/9781644903131-130

Impact of self-heating during hot deformation in the post-dynamic recrystallization and grain growth of an Fe-based superalloy

POTENCIANO Antonio[1,a *], BERNACKI Marc[1,b], NICOLAY Alexis[1,c], COLLIN Cyrille[1,d], DAIRON Jonathan[2,e], DANYLOVA Olena[2,f] and BOZZOLO Nathalie[1,g]

[1]Mines Paris, PSL University, Centre for material forming (CEMEF), UMR CNRS, 06904 Sophia Antipolis, France

[2]Aperam Alloys, 58160 Imphy, France

[a]antonio.potenciano_carpintero@minesparis.psl.eu, [b]marc.bernacki@minesparis.psl.eu, [c]alexis.nicolay@minesparis.psl.eu, [d]cyrille.collin@minesparis.psl.eu, [e]jonathan.dairon@aperam.com, [f]olena.danylova@aperam.com, [g]nathalie.bozzolo@minesparis.psl.eu

Keywords: Self-Heating, Microstructure, Recrystallization, Superalloy, Gleeble

Abstract. During hot working, strain rate, strain level and the temperature of deformation, and hence the Zener-Hollomon parameter, become the regulatory thermomechanical parameters of the resultant stored energy value and distribution. An accurate estimation of the aforementioned parameters is thus required to control microstructural homogeneity in the post-dynamic state, since stored energy value and distribution directly affects post-dynamic recrystallization and grain growth mechanisms. In order to do so, the self-heating phenomena that becomes significant at high strain rate hot deformation must be taken into consideration. In this work, several cylindrical samples of the A-286 alloy are submitted to hot compression tests performed in a Gleeble 3500 machine. The microstructure in the deformed-state is analyzed at the center, and the effect of the thermomechanical parameters of hot deformation on the resulting microstructure is discussed. In addition to this, the local thermomechanical testing conditions are estimated considering self-heating and local strain level and strain rate fields. Hence, the relationship between these newly estimated parameters and the microstructure can be assessed.

Introduction

Fe-based superalloys constitute a cost-effective alternative to Ni-based superalloys, operating in a range of less extreme temperatures. In this context, the A-286 alloy is a Fe-based superalloy employed in the manufacture of various engine and gas turbine components for a wide range of sectors, including aeronautics, automotive, hydrogen power generation, and oil & gas [1-2], for applications in harsh environments. Hence, fine and homogeneous microstructures are required in order to guarantee mechanical properties stability, optimizing the in-use performance and durability of mechanical components. Along the manufacturing route, after successive hot deformations and a subsequent quenching as part of a hot rolling process, this alloy is submitted to a solution heat treatment. This annealing provides good formability, for the sake of recrystallization for further deformation steps, or for the sake of alloying element solutioning prior to controlled precipitation hardening. Under certain specific conditions, heterogeneous grain growth can be activated during the aforementioned heat treatment.

It is known that static recrystallization can be onset in the presence of stored energy, whose value and distribution have a direct impact on the resulting grain size. Store energy is, in turn, dependent on the thermomechanical parameters of hot deformation. During high strain rate hot deformation, significant self-heating can occur. Several hot compression tests, in adiabatic

conditions [3-4], are performed in a Gleeble 3500 machine, covering a wide thermomechanical window where noticeable self-heating phenomena and an acceleration of dynamic recrystallization kinetics is expected. With the aim to reproduce industrial processing conditions, Joule heating can be stopped during the compression stage, due to the compensatory effect of self-heating phenomena at the tested conditions and due to the high strain rate at which the tests are conducted which results in a fast deformation with no time for a cool down.

In order to assess the thermomechanical parameters of hot deformation that will be discussed in the present work, a single parameter is often used to represent the combined effects of strain rate ($\dot{\varepsilon}$) and deformation temperature (T, in K): the Zener–Hollomon parameter (Z) [5], defined as:

$$Z = \dot{\varepsilon} \cdot exp\left(\frac{Q}{RT}\right) \quad (1)$$

where R ($\mathrm{J \cdot mol^{-1} \cdot K^{-1}}$) is the gas constant and Q ($\mathrm{J \cdot mol^{-1}}$) stands for the activation energy for hot deformation.

Dynamic and post-dynamic recrystallized grain size is a direct consequence of plastic stored energy [6]. Recrystallized grain size is then a microstructural parameter of interest in which the effects of the thermomechanical parameters of hot deformation can be analyzed. Derby's law presents a power-law relationship between recrystallized grain size and Zener-Hollomon parameter [7]:

$$D_{RX} = aZ^b \quad (2)$$

with a, b two constant coefficients.

Hence, this article presents an analysis of Derby's law with respect to different Zener-Hollomon parameter estimations (considering self-heating or not), by which it would be possible to discuss the impact of self-heating on the deformed-state microstructure of the A-286 alloy and the relevance of considering it when describing dynamic and post-dynamic microstructural evolutions. Therefore, this article aims to establish a link between the thermomechanical processing conditions and the metallurgical parameters of interest for heterogeneous grain growth in static conditions.

A specific nomenclature will be used to identify whether self-heating is taken into account or not in parameter value estimation:

- $Z_0(\dot{\varepsilon}_n, T_n)$ and ε_n -also expressed as $Z_0(\dot{\varepsilon}_{nominal}, T_{nominal})$ and $\varepsilon_{nominal}$- refer to the nominal Zener-Hollomon parameter value and nominal strain level, respectively, at which the thermomechanical test is desired to be performed.
- $Z_1(\dot{\varepsilon}_f, T_{SH})$ and ε_{SH} represent the estimated value at the end of deformation, considering self-heating, with $\dot{\varepsilon}_f = \varepsilon_{SH}/t_{compression}$. They correspond to the local values at the same central region of the sample at which microstructural observations are performed (Fig. 2).
- $Z_2(\dot{\varepsilon}_n, T_i)$ refers to the local values at the same central region of the sample as before, but T_i is the temperature reached at the last deformation-free stage previous to the compression, without any possible self-heating effect.

- $Z_3(\dot{\varepsilon}_f, T_i)$ differs from $Z_2(\dot{\varepsilon}_n, T_i)$ in the strain rate value considered. In this case, local strain rate at the end of the deformation ($\dot{\varepsilon}_f = \varepsilon_{SH}/t_{compression}$) is used.

Material and experimental procedure

All experiments were conducted on cylindrical specimens (⌀10 mm x L12 mm) sectioned from a 10mm diameter hot rolled bar of A-286 alloy, whose chemical composition is given in Table 1.

Table 1. A-286 superalloy chemical composition.

Elem.	Fe	Ni	Cr	Ti	Mo	V	Mn	Si	Al	C	S	B
% Wt.	Base	27.00 – 24.00	16.00 – 13.50	2.35 – 1.90	1.50 – 1.00	0.50 – 0.10	< 2	< 1.0	< 0.35	< 0.08	< 0.03	< 0.01

The samples are submitted to a specific thermomechanical path to ensure that the microstructure in the state previous to the compression is homogeneous and fully recrystallized (Fig. 1). This is achieved by means of an initial 5 minutes heat treatment in the Gleeble machine at a temperature above the testing temperature (T_{test}), followed by a sudden temperature descent for a 1-minute-long holding at T_{test}. The tests are carried out at high strain rates $\dot{\varepsilon}_{nominal} \in [20, 80]s^{-1}$ and different strain levels $\varepsilon_{nominal} \in [0.25, 0.8]$.

Metallographic preparation and microstructural characterization

After hot compression, samples were cut into identical quarters, aiming to save material and to be able to analyze the microstructure both in the compressed-state and after a final annealing process. The cut was made across the compression direction, *i.e.* the longitudinal direction of the deformed cylinder. Microstructure analyses were made as near as possible to the center of the sample (at around 150 µm distance to the center in the compression direction) in both cylindrical axes considering that a quarter of the original specimen was utilized. Metallographic surface preparation was carried out by means of an initial grinding using SiC abrasive papers down to a SiC granulometry of 5 µm, and then a mechanical polishing step using 3 µm diamond suspension. For optical microscopy observations, the preparation is completed by an electrochemical etching during 100 s at 1 V using HNO_3 (67%) to reveal grain boundaries. In order to obtain an adequate surface quality for scanning electron microscopy (SEM) and electron backscattered diffraction (EBSD) analyses, a final step after mechanical polishing consisting on an electropolishing for 4 s with a A3 Struers electrolyte and operating voltage of 25 V at 25 °C was considered.

EBSD maps were acquired using a Carl Zeiss Supra 40 field emission gun scanning electron microscope (FEGSEM) equipped with a Bruker Quantax system comprising an EBSD e$^-$ FlashHR detector and the Esprit 2.1 software package. Step size was selected considering the dimensions of the scanned area and microstructure characteristic sizes, between 1.2 µm to 2.6 µm per pixel. The acceleration voltage was 20 kV, and the working distance was 15 mm. The open-source MTEX toolbox version 5.1.1 was used for the post-processing of EBSD data [8], using Matlab version R2018a. The high indexing rate, above 98%, indicated that no data cleaning was necessary. Grains must be composed by more than 3 pixels, with a lower threshold of 10° misorientation angle to define grain boundaries. Twins are identified by a 60° misorientation along the axis <111> with a 5° tolerance. All EBSD data were filtered using the half-quadratic filter developed by Bergmann et al. [9] to reduce measurement noise. The half-quadratic filter effectively removes the spatially independent noise from the orientation measurement data while maintaining the sharp gradients at the grain boundaries and subgrain boundaries [10]. Scanning electron micrographs were obtained using the backscattered electron detector with 12 kV voltage at a working distance of 10 mm. The orientation data is represented

by the Kernel Average Misorientation (KAM) parameter. The KAM parameter is a value assigned to each pixel/point in the EBSD map that indicates the average misorientation angle between that pixel and its neighbors. It can be expressed mathematically by the following formula:

$$KAM(p_i) = \frac{1}{v_i}\sum_{j=1}^{v_i} \theta_{i,j} \quad , \tag{3}$$

where $\theta_{i,j}$ is the misorientation angle between pixel p_i and pixel p_j, and v_i is the number of neighboring pixels. For the calculation of KAM, only first and second order neighbors will be considered, and misorientations above 10°, that correspond to grain boundaries, are ignored.

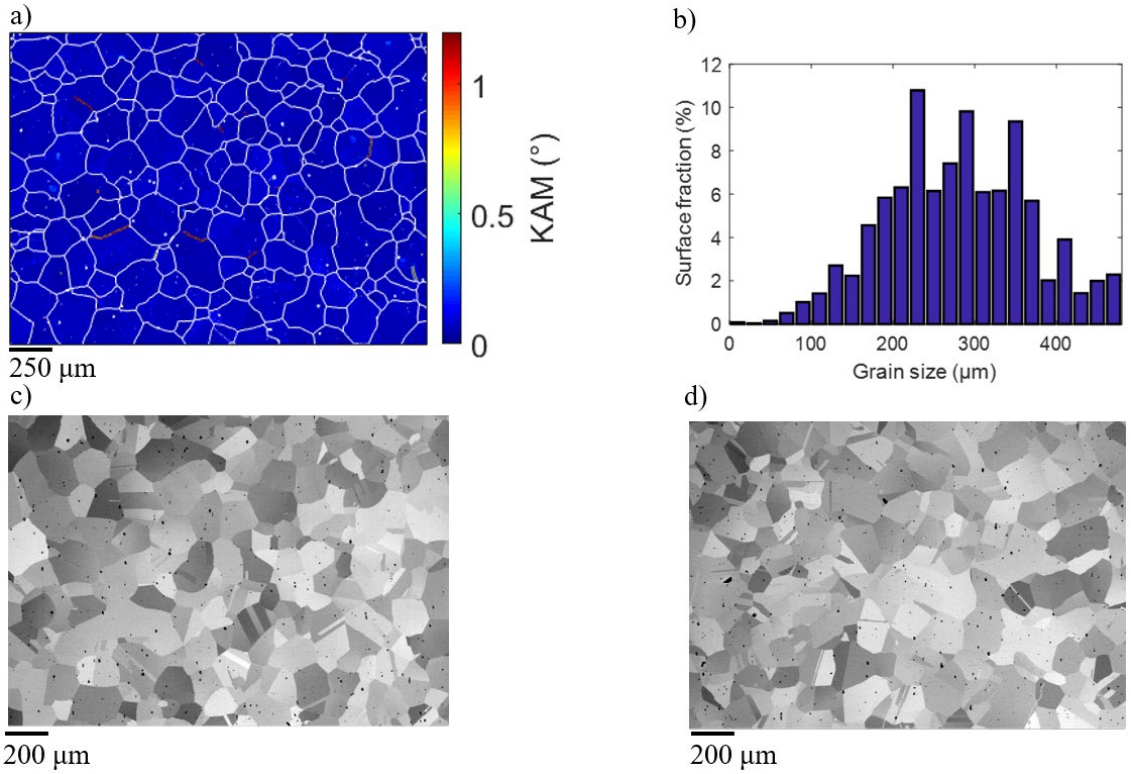

Fig. 1. a), c) and d) Microstructure in the state previous to hot compression, after an initial 5-minutes-long heat treatment and a 1-minute-long heat treatment at the test temperature, in the Gleeble. a) 2nd order KAM map with grain boundaries in white (defined by a misorientation angle higher than 10°). b) Grain size surface fraction histogram. c) and d) Backscattered electrons SEM images, with TiN or TiC as the black second phase particles.

Initial microstructure before compression

In Fig. 1 c and Fig. 1 d, it can be seen that there are second-phase particles uniformly distributed across the microstructure, which correspond to titanium carbides or titanium nitrides. With $\bar{d}_{SPP} = 5.6$ µm and $f_{SPP} = 0.4\%$, they are not expected to be capable of significantly hindering grain boundary migration during thermomechanical processing, and thus they do not have a relevant impact on dynamic and post-dynamic microstructural evolutions with respect to other attributes such as stored energy value and distribution, as proven for similar materials [11]. It is worth mentioning that this microstructure has undergone an initial heat treatment in the Gleeble machine as indicated before. In various works, it has been reported that the Joule effect heating mode of Gleeble has an impact on the microstructure, and hence an electric current flow through

Materials Research Proceedings 41 (2024) 1171-1181 https://doi.org/10.21741/9781644903131-130

a sample has an influence on several solid-state transformations, accelerating recrystallization and precipitation kinetics with respect to conventional radiative systems [12-13].

Hot compression tests

Three thermocouples are spot-welded on the surface of the cylindrical sample. The temperature is controlled by the regulatory thermocouple located at the middle height of the sample (TC2 in Fig. 2), while the two remaining thermocouples are located at a distance of approximately 1 mm to each respective sample edge. These last two thermocouples allow to have a better control of the temperature gradient along the cylinder axis of the sample. The position of the thermocouples along the longitudinal axis must be measured for each sample. The module HydraWedge®, available in the Gleeble 3500 machine, is used, which allows to carry out high strain rate hot compression tests, up to 100 s^{-1}, with good force-displacement control. However, it presents the following drawbacks: strain is measured indirectly via anvil displacement; there are non-negligible friction forces between the anvils and the sample; there is an axial temperature gradient which can vary significantly, with temperature differences up to 25 °C between the mid-height thermocouple and the "edge" ones. Graphite foils of a total width of 0.25 mm are adhered to the interfaces between the end of the sample and each anvil for lubrication purposes. As mentioned in the section *Introduction*, Joule heating is switched off during compression. Immediately after deformation, a Helium quenching is applied, which results in a cooling rate of approximately 40 °C/s.

FE simulations of hot compression tests

The compression tests are simulated with the aim to estimate the local thermomechanical conditions at the center of the specimen, considering self-heating. Forge® software is used [14]. Before the start of compression, there is an initial iterative step to reproduce the experimental temperature profile by adjusting the heating power. Therefore, an analytical thermal model is developed to accurately estimate sample temperature before compression by coupling the thermal and electrical analyses. The tungsten carbide anvils are also modeled, as shown in Fig. 2. A triangular mesh of size 0.2 mm is applied in the sample, except for a region comprising from sample edges up to a 1 mm distance from them, where the mesh is more refined (mesh size of 0.1 mm). The anvils are also meshed. The temperature field on the sample is defined as follows:

-Along the compression direction, at the surface of the sample, a parabolic temperature profile is approximated to the profile captured experimentally by the three aforementioned spot-welded thermocouples. The procedure to accurately reproduce the experimental temperature profile at the surface of the sample will be described next.

-Along the radial direction, a parabolic temperature profile is estimated by means of the average surface temperature of the sample (calculated from the longitudinal temperature distribution) and the thermophysical properties of the material. Knowing that the temperature axial distribution on the surface of the sample is given by the expression $T_{surface}(z) = a_0 z^2 + b_0 z + c_0$, where a_0, b_0 and c_0 are constants determined by the thermocouple data, the temperature at any point of the sample is given by:

$$T(r,z) = T_{surface}(z) + \frac{\sigma_{SB}\varepsilon_R\left(\bar{T}_{surface}^4 - T_0^4\right)}{2\lambda R_0} \cdot (R_0^2 - r^2), \quad (4)$$

where σ_{SB} is the Stefan-Boltzmann constant, ε_R is the material emissivity, λ stands for the thermal conductivity of the material, R_0 is the radius of the sample just before compression, $\bar{T}_{surface}$ is the average temperature on the surface of the sample and T_0 is the room temperature.

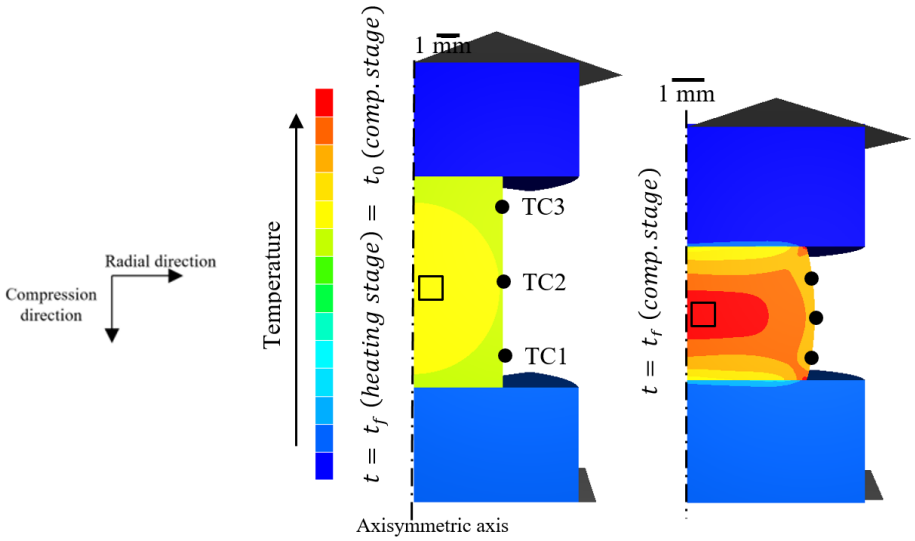

Fig. 2. In the left, temperature field of the sample and the anvils at the end of the heating stage. In the right, temperature field of the sample and the anvils at the end of the compression stage. The square in black corresponds approximately to the region where the microstructure is characterized. Only a quarter section of the axysimmetric specimen is shown in this figure.

Moreover, during the stage of temperature set-up previous to compression, the Joule heating power P_{Joule} (W) can be described as follows, in order to account for radiation and axial anvil conduction losses [15-16]:

$$P_{Joule} = -\int_{\partial\Omega} \overrightarrow{\nabla T} \cdot \vec{n}\, d(\partial\Omega). \tag{5}$$

Using a constant approximated value of the heat transfer coefficient $h\ (Wm^{-2}K^{-1})$ in the interface between the anvil and the specimen, and hence estimating the anvil temperature $\bar{T}_{anvil}$ via the expression $h\left(\bar{T}_{sample\ edge} - \bar{T}_{anvil}\right) = \pm\lambda \cdot \frac{\partial T}{\partial z}\Big|_{z=0,l}$, the value of the power density $\dot{Q}^0_{Joule}\ (Wm^{-3}) = P_{Joule}/(\pi l_0 R_0^2)$ is adjusted iteratively until reaching a good accordance with the experimental temperature profile described by thermocouple data (a difference of less than a 1% of the thermocouple-measured temperature between experimental and simulation data is required to validate the power density ($\dot{Q}^0_{Joule}$) value used for the heating simulation). Hence, the simulations consist of an initial heating stage to adjust the power density value to the experimental axial surface temperature profile, and a final compression stage where $\dot{Q}^0_{Joule} = 0\ Wm^{-3}$ (Fig. 2). For the compression stage, a Coulomb-Tresca friction model has been used for the interface between the sample and the anvils. A rheological model for the A-286 alloy under hot compression calibrated from several experiments is utilized. Concerning the estimation of sample dimensions, it is worth indicating that thermal expansion is taken into account, as described below, since the dependence of mass density $\rho(T)$ with temperature is known for the alloy [15]:

$$l(T_{test}) = l_0(T_0)\left(\frac{\rho(T_0)}{\rho(T_{test})}\right)^{\frac{1}{3}} \tag{6}$$

The expression in Eq. 6 is used to estimate the length of the sample $l(T_{test})$ by only considering thermal expansion at test temperature. It is also used to estimate the radius of the

sample $r_0(T_{test})$ at a given time, by replacing l for r. Moreover, this expression is used to calculate the final length that the sample must reach for the compression to stop $l_f(T_f)$. The final dimensions of the compressed specimen are measured at room temperature, thus, in the simulation of the compression stage, the anvil (and hence the sample) follows the experimental jaw displacement, from the initial calculated dimensions of the sample (in Eq. 7) to the final thermally corrected length of the sample, to compensate for the elastic correction. Sample dimensions at the end of the heating stage, just before compression, are estimated considering both thermal expansion and creep, so the formula in Eq. 6 is combined with the displacements captured by the LVDT gauge as defined in Fig. 3 associated to creep, Δl_1^{creep} and Δl_2^{creep}, as follows:

$$l_0 = \left(\frac{\rho(T_{plateau})}{\rho(T_{compression})}\right)^{\frac{1}{3}} \cdot \left(\left(\frac{\rho(T_0)}{\rho(T_{plateau})}\right)^{\frac{1}{3}} l_0(T_0) - \Delta l_1^{creep}\right) - \Delta l_2^{creep}. \quad (7)$$

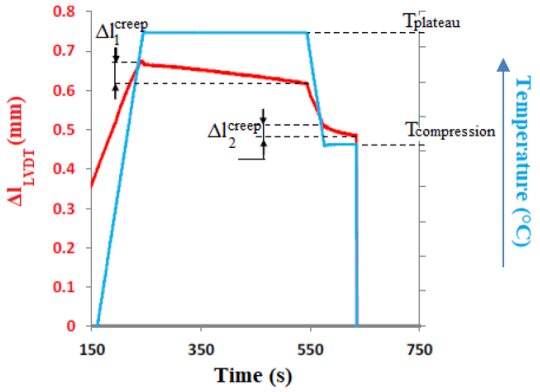

Fig. 3. Temperature evolution and length variation (captured by the LVDT gauge) of a sample during the thermal path followed before compression, indicating the effect of creep.

Results and discussion

After Gleeble hot compression, all the deformed-state microstructures analyzed can be classified in three types according to their recrystallized fraction (f_{RX}), as shown in Fig. 4:

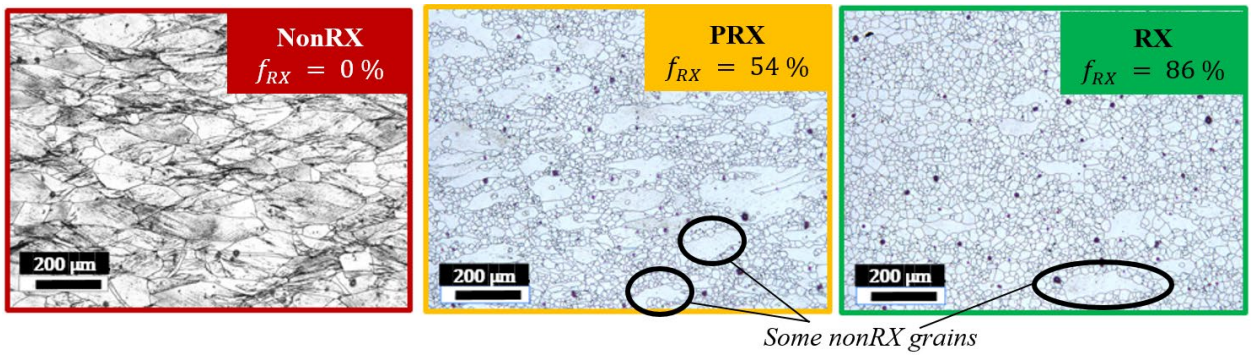

Fig. 4. Optical microscopy images (after an electrochemical etching to reveal grain boundaries as described in the section Metallographic preparation and microstructural characterization) of three different microstructures representatives of each class: Non-recrystallized microstructures (NonRX), with $f_{RX} \leq 10\%$; partially recrystallized microstructures (PRX), with $10\% < f_{RX} < 80\%$; recrystallized microstructures (RX), with $f_{RX} \geq 80\%$.

Materials Research Proceedings 41 (2024) 1171-1181 https://doi.org/10.21741/9781644903131-130

In all the optical microscopy images of the compressed microstructures, non-recrystallized grains and hence f_{RX} are identified by imaging processing software by implementing specific criteria of high grain size and non-equiaxiality aspect ratio for each microstructure (Fig. 4). The size and density of recrystallized grains in the state after compression, which will have an impact on static microstructural evolutions, depend on the thermomechanical parameters of deformation. Fig. 5 shows the relationship between thermomechanical parameters of deformation, such as the local strain level (ε_{SH}) and the different Zener-Hollomon parameter estimations, and the microstructure *via* the f_{RX} range at which it belongs (according to the color code of the data points). In addition to this, the relationship between $ln(Z)$ and ε_{SH} allows to evaluate the accuracy of the different estimations of the Zener-Hollomon parameter.

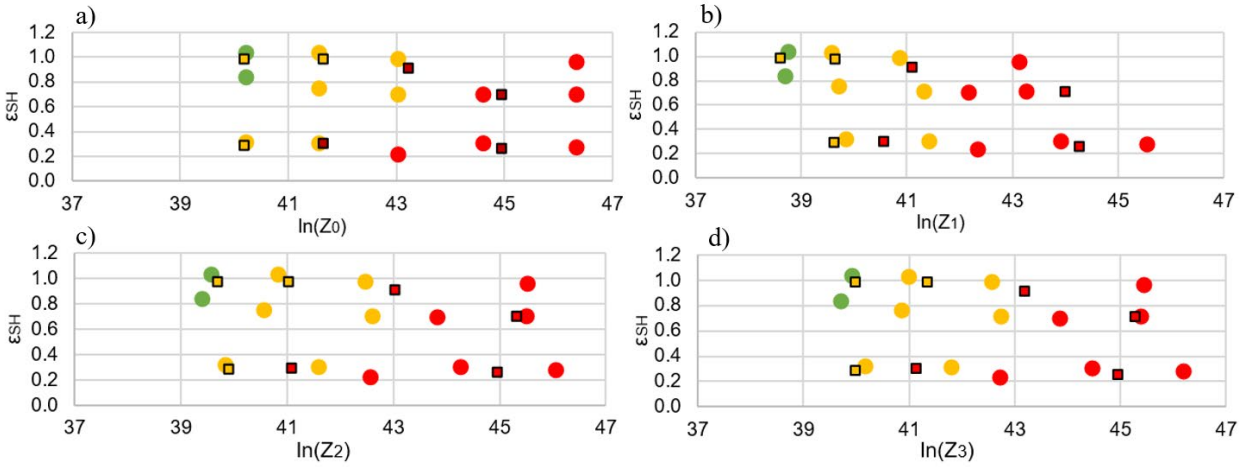

Fig. 5. Local strain level at the center of the sample (ε_{SH}) vs. Zener-Hollomon parameter calculated from (see section Introduction for the detailed description of the different estimations of the Zener-Hollomon parameter) a) nominal global values b) local values after compression c) local values before compression, with no self-heating phenomena considered and nominal strain rate d) local temperature before compression and local strain rate after compression. Circle mark points refer to the tests performed at $\dot{\varepsilon}_n = 80\ s^{-1}$ while square marks stand for the tests carried out at $\dot{\varepsilon}_n = 20\ s^{-1}$. Additionally, the colors (green, yellow and red) are consistent with the criteria defined in Fig. 4 to identify different microstructure types according to f_{RX} (recrystallized, partially recrystallized and non-recrystallized microstructures, respectively).

The use of local parameters instead of nominal estimations in the calculation of the Zener-Hollomon parameter results in a better distribution of points according to their microstructure type (f_{RX} range) in Fig. 5 b with respect to Fig. 5 a. The use of nominal parameters in Z_0 calculation is not as predictive of the compressed-state microstructure as the use of local temperature estimations in Z_1, Z_2 and Z_3 calculation. This is shown in Fig. 5 a, where identical Z_0 values are shared by conditions with very different f_{RX} values (according to data point color). However, the consideration of self-heating (Fig. 5 b) or not (Fig. 5 c and Fig. 5 d) in Zener-Hollomon parameter calculation has less impact on the arrangement of data points according to their color, as it can be seen from the few differences among these graphs. For both the tests performed at $\dot{\varepsilon}_n = 80\ s^{-1}$ (circle data points) and the tests performed at $\dot{\varepsilon}_n = 20\ s^{-1}$ (square data points), it can be seen that the arrangement of points according to their f_{RX} value is slightly better defined in Fig. 5 b: high strain and low Zener-Hollomon parameter tests yield a fully recrystallized microstructure, while low strain and high Zener-Hollomon parameter tests yield a non-recrystallized microstructure.

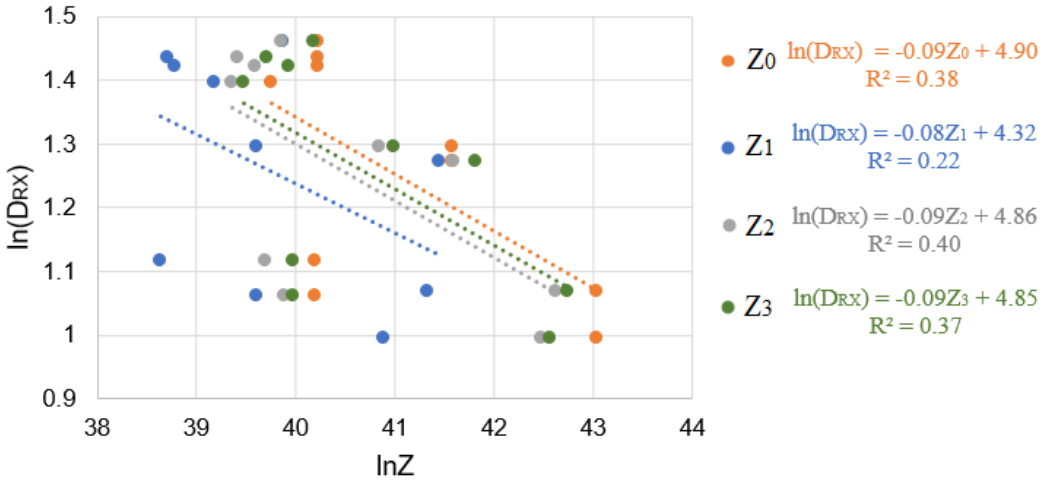

Fig. 6. Logarithmic relation between the recrystallized grain size (D_{RX}) and the different estimations of the Zener-Hollomon parameter (Z). A least squares linear regression line (dotted line) and the coefficient of regression R^2 is shown for every set of points corresponding to a different Zener-Hollomon parameter estimation.

The relationship between recrystallized grain size and Zener-Hollomon parameter can be found in Fig. 6. It can be observed that there is no correlation for any of the different Zener-Hollomon parameter estimations analyzed, as the R^2 coefficients indicate. For the hot-deformed A-286 alloy at $\dot{\varepsilon}_{nominal} \in [20, 80] s^{-1}$, Derby's law fails to establish a relationship between the thermomechanical parameters of deformation and recrystallized grain size. The consideration of local self-heating at the end of deformation in the calculation of Z_1 results in a higher dispersion of the results with respect to recrystallized grain size, which suggests that the estimated self-heating phenomena does not have an impact on dynamic and post-dynamic grain growth, in contrast with the results found in Fig. 5 regarding recrystallization with respect to local strain level.

Conclusion

Self-heating during hot deformation, especially at high strain rate, must be taken into account to assess plastic stored energy value and distribution in order to correctly predict static recrystallization and grain growth mechanisms. The mastering of static microstructural evolutions in the A-286 alloy would allow to predict the formation of heterogeneous microstructures in static conditions. The power-law relationship between recrystallized grain size (a consequence of stored energy) and Zener-Hollomon parameter as defined in Derby's law is sensitive to the use of local thermomechanical values instead of the nominal ones. However, local temperature and strain rate at the end of deformation do not share a correlation with the recrystallized grain size obtained after hot compression tests at high strain rate ($\dot{\varepsilon}_{nominal} \geq 20\ s^{-1}$). The most accurate estimation of the thermomechanical parameters of hot deformation to better predict dynamic and post-dynamic microstructural evolutions is still open to discussion, and a question now arises about which is the most microstructure-impactful moment in the thermomechanical path during the hot compression process, since the thermomechanical conditions at the end of deformation are not representative enough of the resulting compressed-state microstructure. The microstructures obtained from high strain rate Gleeble testing differ from those obtained from testing at lower strain rates due to a lower dislocation density and different intragranular dislocation distributions, so the link between the thermomechanical parameters of deformation and the deformed-state microstructure as stated by Derby would no longer be valid. Furthermore, the lack of a Derby relationship at these conditions could suggest

that post-dynamic recrystallization and grain growth have a bigger impact in the resulting microstructure than dynamic evolutions.

Acknowledgements
This study was carried out with Aperam funding and support, in the frame of the DIGIMU consortium, handled by MINES Paris and Armines.

References

[1] X. Huang, J. Li, B.S. Amirkhiz, P. Liu, “Effect of water density on the oxidation behavior of alloy A-286 at 625 °C - A TEM study”, Journal of Nuclear Materials, 2015, vol. 467, pp. 758-769. https://doi.org/10.1016/j.jnucmat.2015.10.023

[2] O. Takakuwa, Y. Ogawa, J. Yamabe, H. Matsunaga, “Hydrogen-induced ductility loss of precipitation-strengthened Fe-Ni-Cr based Superalloy”, Materials Science & Engineering A, 2019, vol. 739, pp. 335-342. https://doi.org/10.1016/j.msea.2018.10.040

[3] A. Nicolaÿ, J.M. Franchet, J Cormier, H. Mansour, M. de Graef, A. Seret, N. Bozzolo, “Discrimination of dynamically and post-dynamically recrystallized grains based on EBSD data: application to Inconel 718.”, Journal of Microscopy, (2018), Vol. 00, pp. 1-13. https://doi.org/10.1111/jmi.12769

[4] Sela, A., Ortiz-de-Zarate, G., Soler, D., Germain, G., Gallegos, L., & Arrazola, P. J. “Adiabatic self-heating determination for Ti6Al4V at different temperatures.”, International Journal of Heat and Mass Transfer, 2023, 204, 123747. https://doi.org/10.1016/j.ijheatmasstransfer.2022.123747

[5] Zener, Clarence, and John Herbert Hollomon. "Effect of strain rate upon plastic flow of steel." Journal of Applied physics 15.1 (1944): 22-32. https://doi.org/10.1063/1.1707363

[6] Rollett, Anthony, Gregory S. Rohrer, and John Humphreys, Recrystallization and related annealing phenomena, Newnes, 2017.

[7] B. Derby, The dependence of grain size on stress during dynamic recrystallisation. Acta metallurgica et materialia, 39(5), (1991) 955-962. https://doi.org/10.1016/0956-7151(91)90295-C

[8] Bachmann, F., Hielscher, R., & Schaeben, H. (2011). “Grain detection from 2d and 3d EBSD data—Specification of the MTEX algorithm”, Ultramicroscopy, 2011, 111(12), 1720-1733. https://doi.org/10.1016/j.ultramic.2011.08.002

[9] Bergmann R, Chan RH, Hielscher R, Persch J, Steidl G “Restoration of manifold-valued images by half-quadratic minimization”, Inverse Probl. Imaging, 2016, 10:281–304. https://doi.org/10.3934/ipi.2016001

[10] Lehto, P., & Remes, “EBSD characterisation of grain size distribution and grain sub-structures for ferritic steel weld metals” Welding in the World, 2022, 66(2), 363-377. https://doi.org/10.1007/s40194-021-01225-w

[11] A. Agnoli, M. Bernacki, R. Logé, J.-M. Franchet, J. Laigo, N. Bozzolo, “Selective growth of low stored energy grains during δ sub-solvus annealing in the Inconel 718 nickel-based superalloy”, Metallurgical and Materials Transactions A, 2015, vol. 46, pp. 4405–4421. https://doi.org/10.1007/s11661-015-3035-9.

[12] A. Nicolaÿ, J.M. Franchet, J Cormier, R. E. Logé, G. Fiorucci, J. Fausty, M. Van der Meer, N. Bozzolo, "Influence of Joule effect heating on recrystallization phenomena in inconel 718.",

Metallurgical and Materials Transactions, A 52.10 (2021), 4572-4596. https://doi.org/10.1007/s11661-021-06411-5

[13] H. Conrad, "Effects of electric current on solid state phase transformations in metals." Materials Science and Engineering, A 287.2 (2000), 227-237.

[14] P. de Micheli, A. Settefrati, S. Marie, J. Barlier, P. Lasne, et al. “Towards the simulation of the whole manufacturing chain processes with FORGE,” in Proc. Int. Conf. on “New development in forging technology,” 2015, pp. 1–25.

[15] Carlslaw, H. S., and J. C. Jaeger. "Conduction of Heat in Solids." Oxford University Press, Oxford (1959).

[16] Evans, R. W., and P. J. Scharning. "Axisymmetric compression test and hot working properties of alloys." Materials science and technology 17.8 (2001), 995-1004. https://doi.org/10.1179/026708301101510843